
LIGHTCONVPOINT: CONVOLUTION FOR POINTS

Alexandre Boulch, Gilles Puy, Renaud Marlet
valeo.ai, Paris, France

ABSTRACT

Recent state-of-the-art methods for point cloud semantic segmentation are based on convolution defined for point clouds. In this paper, we propose a formulation of the convolution for point cloud directly designed from the discrete convolution in image processing. The resulting formulation underlines the separation between the discrete kernel space and the geometric space where the points lies. The link between the two space is done by a change space matrix \mathbf{A} which distributes the input features on the convolution kernel. Several existing methods fall under this formulation. We show that the matrix \mathbf{A} can be easily estimated with neural networks. Finally, we show competitive results on several semantic segmentation benchmarks while being efficient both in computation time and memory.

1 Introduction

Convolutional Neural Networks (CNNs) have been a breakthrough in machine learning for image processing [7, 18]. By cascading convolutional layers, it is possible to progressively build various representations of the data, from local neighborhood descriptions to high-level task-oriented features. Besides, the discrete formulation of the convolution allows a very efficient processing of grid-structured data such as images in 2D or videos in 3D. However, a number of tasks make use of unstructured data such as point clouds, graphs or meshes, with application domains such as autonomous driving, building information model (BIM) reconstruction, animation or visualization. The problem is that discrete convolutions cannot directly apply to point clouds as points are not usually sampled on a grid.

The most straightforward approach to apply convolution on unstructured data is to recover some form of structure by reorganizing the data, i.e., by voxelizing a point cloud [27]. However, as points are usually sampled on a surface, most of the voxels are empty, which leads to memory and processing inefficiencies. A treatment of sparsity is required [34, 56].

Other approaches propose to generalize machine learning techniques to unstructured data. Deep network on graphs [38] and geometric deep learning [6] define convolutional operators that can be used on meshes using the neighboring relations between points defined by a graph. However, when using point clouds, the application of these methods may be problematic due to the difficulty to define a relevant mesh or graph relating the points (neither too many nor too few connections), which implies in practice having also priors on the data (e.g., sampling of a surface).

Deep-learning techniques that directly process raw data have been developed to overcome the problems of point cloud preprocessing [30, 47]. Just as for structured data, such networks are usually designed as a

LightConvPoint code is available on the valeo.ai github: <https://github.com/valeoai/LightConvPoint>

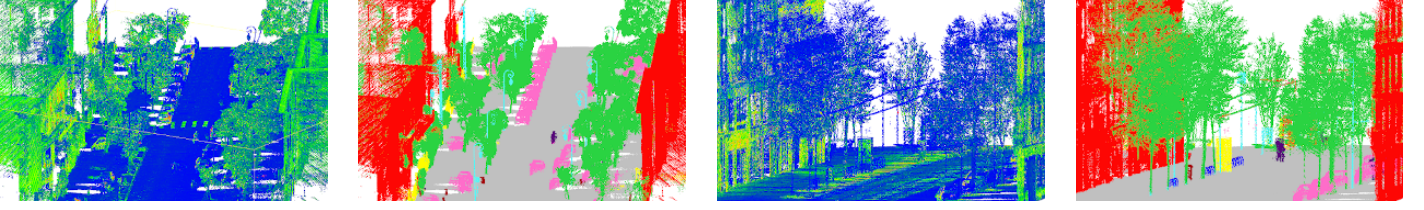


Figure 1: Visual results for semantic segmentation on the NPM3D test dataset, input data (colored according to lidar intensity) and segmentation result.

stack of layers and are optimized using stochastic gradient descent and back-propagation. Key issues when designing these networks include speed and memory efficiency.

In this context, we propose a new convolution method for point cloud processing. It is a mixed discrete-continuous formulation. On the one hand, as point clouds are generally sampled on manifolds in the spatial domain, which is a continuous space, the spatial part of the convolution is also processed in a continuous domain. On the other hand, in the feature space, we stick to the discrete formulation which has been successful for grid data and is memory efficient.

Our contributions are the following: (1) We propose a framework to analyze existing methods and use it to define our own. (2) The new method we propose separates the estimation of the weights of convolution kernels and the estimation of the spatial relation between points and kernels, similar to discrete convolution. (3) Experiments on large-scale datasets for semantic segmentation show that our approach is the first method based on k -nearest neighbors in the benchmarks.

2 Related work

Data projection approaches. A first category of deep learning methods projects the point cloud in a space suitable for the use of discrete convolutional neural networks (CNNs). That is, they project the data on a grid, either 2D (image pixels) or 3D (voxels). 2D CNNs have been used for 3D converted as range images [12, 25] or by placing virtual viewpoints in the scene for classification [41] or semantic segmentation [4, 20]. As neighboring points in the image can be far away in the 3D space, 2D interpretations often fail to capture the 3D relations. At a local scale, 2D CNN can also be applied to point-specific neighborhoods by projecting on the tangent plane [42]; the result is then highly dependant on the tangent plane estimation. Other approaches use a volumetric representation of the data, such as voxels [27, 31, 36, 50]. These approaches suffer from encoding mostly empty volume when dealing with large grids. To overcome these issues, octree-based CNN [34] or sparse convolution have been proposed [10, 11].

Graph convolution and geometric deep learning. Graph-structured data do not lie on regular grid. Graph Neural Networks (GNNs) [23, 33, 38] extend neural networks to graphs, using edges between nodes for message passing. To deal with the difficulties scale to large point clouds, SPG [19] defines a graph over a pre-segmented point cloud, whose segment nodes are described using PointNet [30]; PointNet descriptors and edge features are optimized at the same time during training. Graph convolutions can also be used to hierarchically process graph patches from local features to high-level representations [9, 17, 53]. Often referred to as *geometric deep learning* [6] when applied to manifolds or meshes, deep learning for graphs has developed rapidly over the last years, particularly for shape matching where invariance to surface deformations is required. Extension of CNNs to manifolds includes anisotropic diffusion kernel [3] and the generalization using mixture model CNNs [28]. In contrast, our approach is applied directly to the raw point

clouds with no pre-defined relation between points, thus inherently making the construction of the graph as part of the problem.

Pointwise processing with MLP. Processing the raw point cloud has recently become a mainstream problem with the pioneering work of PointNet [30]. A multi-layer perceptron (MLP) is applied individually over the points and context information is acquired with permutation-invariant max-pooling. PointNet++ [32] and So-Net [21] reduce the local information loss due to subsampling with a cascade of local MLPs from small to large scale.

Convolution on points. Convolution for points has followed as a natural extension of previous work on regular grids and graphs. There are two main lines of work.

A first line of work considers an explicit spatial location for the kernel, located in the same space as the point cloud. The kernel elements can be located in a regular grid (voxels) [15], at the vertices a polyhedron [44] or randomly sampled and optimised at training [5]. In KPConv [44], an adjustment of the kernel locations may also be predicted at inference time to fit better the data. In this work, we use network architectures similar to ConvPoint, and show that our formulation is faster and consumes less memory.

Another type of approaches relies on an implicit modeling of the kernel locations. In SpiderCNN [51], the kernel is a family of polynomial function. In PointCNN [22], the input features are directly aggregated into fewer representative points. While sharing similarities with ours, it does not separate totally the spatial domain from the feature space, which is one of the key aspect of our formulation. PCCN [47] is maybe the work that is the closest to ours, despite its implicit kernel. The weighting of the input features, which implicitly express kernel weights, are directly computed based on the local geometry of the points. In contrast, we learn the weight of a discrete kernel and, at inference time, we only estimate the spatial relations between the kernel and input points.

Our approach lies in between those two lines of work. On the one hand, our kernel weights are explicitly modeled, which gives a discrete flavor to our method; on the other hand, we estimate a transformation of the input points to apply the convolution, as in PCCN, which implies a continuous treatment. The key is that, contrary to PCCN, which re-estimates at inference time how to weight a given a set of points to express the convolution, we estimate separately a kernel while learning and the spatial relations between the kernel and input points while testing, performing convolution with an explicit matrix multiplication rather than getting directly the results from the network output. This separation and the explicit matrix multiplication (outside the network) allows a better learning of kernel weights and spatial relations, without the extra burden and inaccuracy to estimate their composition. As a result, our method is faster and requires less memory.

3 Convolution for point cloud

Our objective is to design a convolutional layer for point clouds, efficient both in memory and computation time. We build our convolution operation based on the discrete convolution, used in image or voxel grid processing. The resulting formulation is general enough to cover a range of state-of-the-art convolution operations for point clouds.

3.1 Discrete convolution

Let F be the input feature space dimension, d be the spatial dimension (e.g., 2 for images, 3 for voxel grid). We denote by \mathbf{K} the convolution kernel, \mathbf{f} the input features. The classical discrete convolution output,

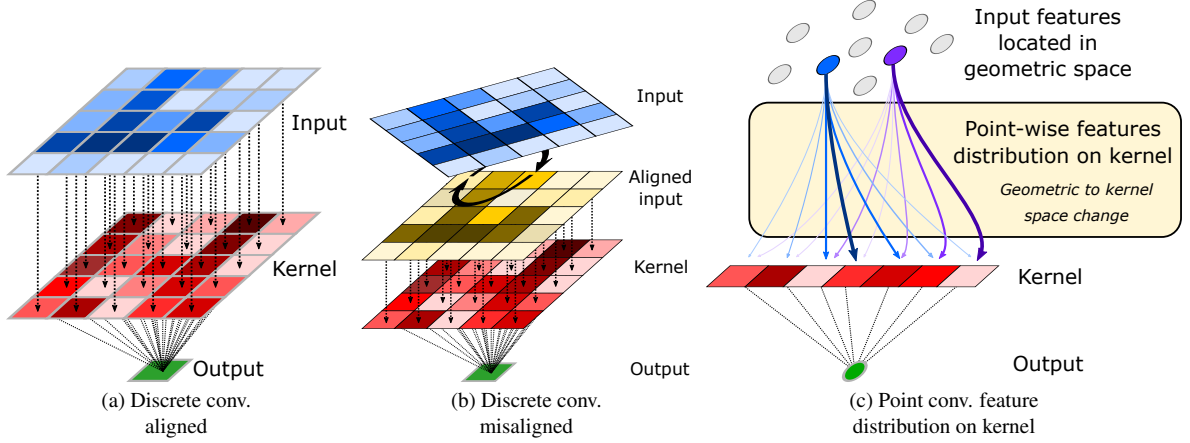


Figure 2: Kernel/Input alignment for grid inputs and point clouds.

denoted by \mathbf{h} , satisfies

$$\mathbf{h}[n] = \sum_{f \in \{1, \dots, F\}} \sum_{m \in \{-M/2, \dots, M/2\}^d} \mathbf{K}_f[m] \mathbf{f}_f[n + m], \quad (1)$$

where M is the kernel size of the grid kernel, f indexes the feature space, n is the spatial index, and $\mathbf{K}_f[m]$ and $\mathbf{f}_f[n + m]$ are scalars.

Let us define the vectors $\mathbf{K}_f = (K_f[m], m \in \{-M/2, \dots, M/2\}^d)$ and $\mathbf{f}_f(n) = (\mathbf{f}_f[n + m], m \in \{-M/2, \dots, M/2\}^d)$, then, equation (1) becomes

$$\mathbf{h}[n] = \sum_{f \in \{1, \dots, F\}} \underbrace{\mathbf{K}_f^\top}_{\text{Kernel space}} \underbrace{\mathbf{f}_f(n)}_{\text{Feature space}}, \quad (2)$$

where we highlight the separation between the kernel space (\mathbf{K}) and the feature space (\mathbf{f}).

3.2 Convolution for continuous points

In discrete convolutions, as the kernel \mathbf{K}_f and the input feature patch $\mathbf{f}_f(n)$ are perfectly aligned, the kernel elements $\mathbf{K}[m]$ have a direct relation with a unique input element $\mathbf{f}_f[n + m]$: they are indexed by m in the same way (figure 2(a)).

To generalize the discrete convolution to point clouds, we now consider a misalignment between the feature and kernel spaces. Let us consider the hypothetical problem where the kernel grid is rotated with respect to the feature grid (figure 2(b)). There is no obvious correspondence between the kernel and input feature elements any more. Nevertheless, provided that the rotation matrix $\mathbf{A} \in \mathbb{R}^{M^d} \times \mathbb{R}^{M^d}$ is known, one can restore the correspondences by operating a change of space from the input to the kernel space with the rotation matrix:

$$\mathbf{h}[n] = \sum_{f \in \{1, \dots, F\}} \mathbf{K}_f^\top \mathbf{A} \mathbf{f}_f(n). \quad (3)$$

This equation holds in a more general setting, with an arbitrary linear transformation between the feature space and the kernel space; \mathbf{A} is then the *assignment matrix* that distributes the feature values to the kernel elements. By using $\mathbf{A} = \mathbf{I}_{M^d}$, the identity matrix, we recover the particular case of the discrete convolution.

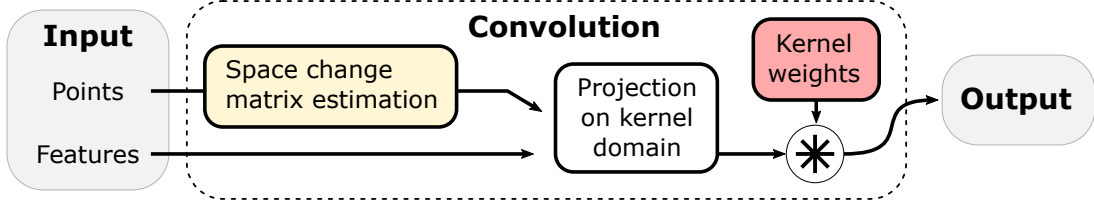


Figure 3: Convolutional layer. \otimes is the elementwise multiplication.

In the case of a point clouds, $\mathbf{f}_f[n]$ is the feature associated to the point at spatial location n computed using a neighborhood $\mathbf{N}[n]$ of size k . These features typically are not grid-aligned. The previous equation still applies, provided that we can estimate an assignment matrix \mathbf{A} which distribute each point to the kernel element (figure 2(c)).

3.3 Estimating kernel-feature relations

A fixed \mathbf{A} matrix is not a sensible choice as it should deal with all possible configurations of the input points, including the discrete case (in which case it shall be the identity). Thus, in the case of a point cloud, \mathbf{A} has to be a function of the input points, which we limit to the neighbors $\mathbf{N}[n]$ at location n . We make \mathbf{A} a function of the neighborhood, $\mathbf{A}(\mathbf{N}[n])$, and the convolution for points becomes:

$$\mathbf{h}[n] = \sum_{f \in \{1, \dots, F\}} \mathbf{K}_f^\top \mathbf{A}(\mathbf{N}[n]) \mathbf{f}_f(n) \quad (4)$$

This formulation is a mixed continuous-discrete convolution: \mathbf{K}_f and $\mathbf{f}_f[n]$ have discrete support and continues values while $\mathbf{A}(\mathbf{N}[n])$ is estimated in the continuous domain. Figure 3 presents the operations involved in our convolutional layer. In practice, this formulation is generic enough to describe most of the formulations for point cloud convolution.

Using spatial kernel points. The most common approach to discrete point cloud convolution is to create a spatial point for each of the kernel elements. It is then possible to compute distances between the kernel points and points in $\mathbf{N}[n]$ and distribute the corresponding features on the kernel accordingly, building an association matrix \mathbf{A} invariant by rotation. A first method is to associate the features to the nearest kernel point. However, this causes a quantization issue as a small variation in the point position may result in a different kernel point attribution. A workaround is to distribute the input to several close kernel points. In SplatNet [40], the authors use an interpolation to distribute the input features to the kernel space. However, this handcrafted assignment is, somehow, arbitrary and heavily relies on the geometry of kernel points. In KPConv [44], the authors propose to distribute the inputs over all the neighboring kernel points, inversely proportionally to the distance between them. Moreover, their formulation allows the use of deformable kernels, in which local shifts of the kernel points are estimated, allowing more flexibility with respect to the input. Yet, this handcrafted distribution is also arbitrary and relies on the geometry of kernel points. A different approach is proposed in ConvPoint [5], where the kernel points are randomly sampled and their position is learned along with the distribution function \mathbf{A} : a multi-layer perceptron (MLP) is applied to the kernel points represented in the coordinate system centered on the input points. All these methods rely on kernel points, coming with the difficulties to position them and/or optimize their position.

Joint estimation of $\mathbf{K}^\top \mathbf{A}(\mathbf{N}[n])$. In PCCN [47], an MLP is used to directly estimate the weight to apply on the input features, *i.e.*, the result of the whole product $\mathbf{K}^\top \mathbf{A}(\mathbf{N}[n])$. This continuous convolution approach mixes the estimation in the spatial domain and the feature domain. However, as acknowledged by the authors themselves in [47], this approach is too computationally expensive to be used in practice. Instead, they adopt

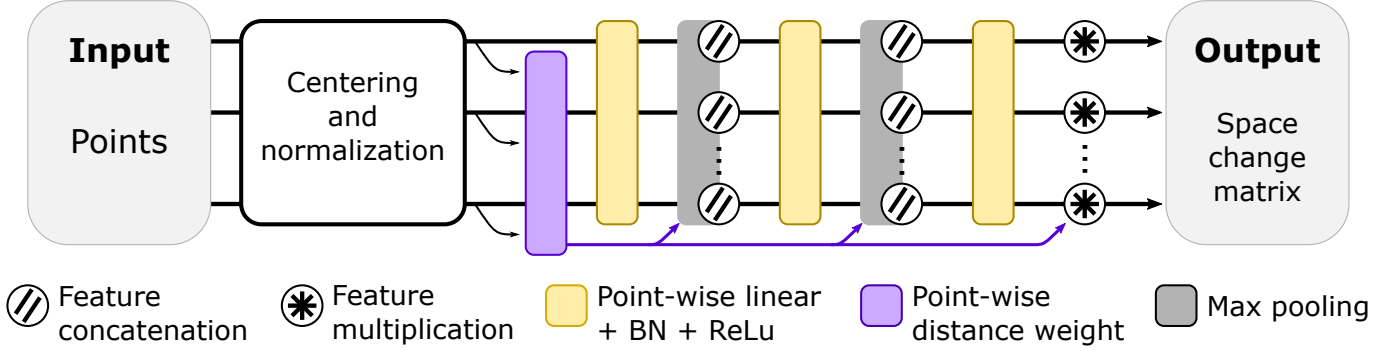


Figure 4: Estimation of the matrix A , link between points and kernel.

an implementation which falls in our formalism, considering N_{out} parallel convolution layers with a size-1 kernel, which corresponds to using a single A for all filters. N_{out} being the number of output channels.

Direct estimation of A . In this work, we do not use kernel points. The soft assignment matrix A is directly estimated based on the coordinates of the neighboring points in $N[n]$. As underlined in [30], a point cloud is invariant by point permutation: shuffling a list of points does not change the point cloud. Hence, the product $A f_f(n)$ must be invariant by permutation of the inputs. It can be achieved by estimating independently each line A_j of the matrix A using the corresponding point $p_j \in N[n]$ only, with an MLP shared across all points. However, this formulation does not take the neighborhood into account. The neighboring points may contain useful information such as the local normal or curvature. To integrate this information, PointNet [30] uses a max pooling operation, which is permutation invariant. In practice, any global pooling operation is agnostic to the spatial position. Inspired by PointNet, we use a three-layer point-wise MLP with max-pooling after the first two layers. The max-pooling output is then concatenated to the point-wise features before the next fully-connected layer.

3.4 Neighborhood normalization

As stated in [44] using neighborhoods defined by a radius instead of a k -nearest neighbors (k -nn) ensure spatial consistency. On the one hand, using a fixed number of neighbors is relatively fast but the radius of the encompassing ball is variable, potentially with high variance, e.g., with lidar point sampling. On the other hand, a radius neighborhood search is a way to tackle this problem. However, it is usually slower than a k -nn search and requires to set up a strategy to deal with variable neighborhood sizes, as in [44] where the tensors sizes are set to large dimensions and neighborhood sizes are tracked during processing.

We propose an intermediary approach. We still search for the k nearest neighbors but, as opposed to [5, 22, 32], we do not normalize all neighborhoods to a unit sphere regardless of the actual size in the metric space. We estimate the normalization radius of the neighborhood at the level of the layer using an exponential moving average:

$$r_t = \hat{r} * m + r_{t-1} * (1 - m) \quad (5)$$

where t is the update step, m is the momentum parameter and \hat{r} is the average neighborhood radius of the current batch. This normalization ensures the neighborhoods to be at the same scale when processed by the convolution layer. However, it does not prevent points far away from the support point (the neighborhood center) to influence the result.

One could use hard-thresholding on the distance based on the estimated normalization radius r , but this approach may cut too much information from the neighborhood, particularly in the case of high variance

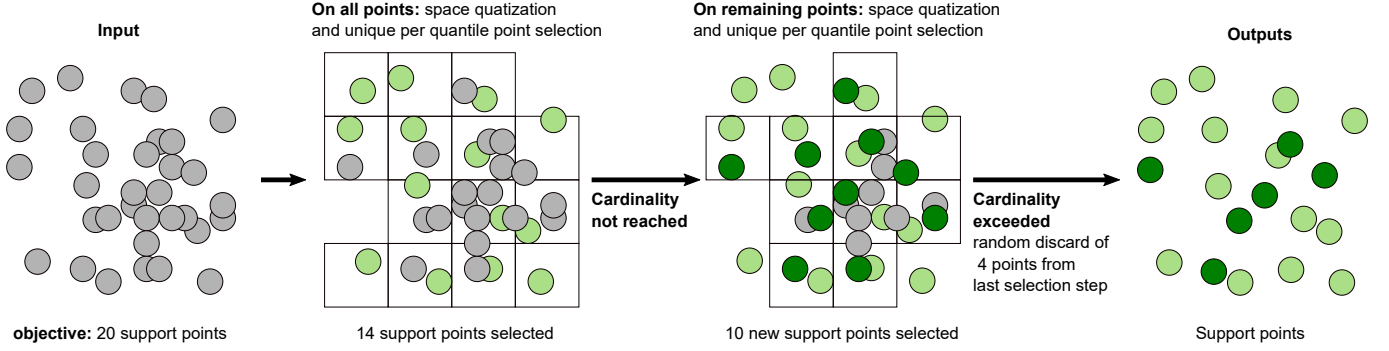


Figure 5: Point sampling with quantization of the space.

in neighborhood radii. Instead, we define a learned weighting function in the form of:

$$w(x) = \sigma(\beta - \alpha x) \quad (6)$$

where $\sigma(\cdot)$ is the sigmoid function, x is the distance to the support point, β is the parameter defining the window size and α is the smoothness factor of the window. α and β are learned. Finally, the rows of \mathbf{A} are weighted according to w to reduce the influence of the neighboring points considered as outliers:

$$A_i \leftarrow A_i * w(d(p_i, q)) \quad (7)$$

where $d(\cdot, \cdot)$ is a distance function, p_i is the i^{th} point of the neighborhood of the support point q .

4 Point sampling

Networks architectures for point cloud processing operates at full resolution through the entire network [47] or have an encoder/decoder structure [5, 22] similar to networks used in image processing, e.g., U-Net [35]. While the former maintain a maximum of information through the network, the later is usually faster as convolutions are applied on smaller point sets. However, decreasing the size of the point cloud requires to select *the support points* (i.e., the points at the center of the neighborhoods used in the convolution).

In PointNet++ [32], the authors introduce farthest point sampling. It is an iterative procedure to sample points where the next sampled point is the farthest point from the already picked points. The main advantage of this approach is to ensure a good spatial sampling of the point cloud, and particularly, favors the selection of extreme points (e.g., wing extremities for planes) which are usually important for shape recognition. However, this sampling requires to maintain the distance map between all points, which is costly and increases the computation times, particularly when dealing with large point clouds.

In ConvPoint [5], the point picking strategy only takes into account seen/unseen points, without distance consideration. Points are randomly picked among points that were not previously seen (picked points and points in the neighborhood of these points). While being much faster than farthest point picking, it appears to be less efficient (see experimental section 5). In particular, the sampling is dependent of the neighborhood size: sampling is done outside neighborhood of previously picked support points. A very small neighborhood size reduces the method to a pure random sampling.

Space quantization

We propose an alternative approach which ensure a better sampling than [5] while being much faster than [32]. The procedure is illustrated in Fig. 5. We discretize of the space using a regular grid, i.e., voxels. Each point

is associated to the grid cube it falls in. In each non-empty grid cube, one point is selected. We continue with the non-selected points and a voxel size divided by two, and repeat the process until the desired number of sampled points is reached or exceeded. In the later case, some points selected at the last iteration are discarded, at random, to reduce the cardinality of Q the set selected points.

Quantization step estimation

Our approach is voxel size dependent. On the one hand, a coarse grid leads to many iterations in the selection procedure, at the expense of computation time. On the other hand, a fine grid reduces the method to random sampling. Finding the optimal size can be achieved using an exhaustive search (search the parameter that lead to $|Q|$ filled voxels for a single quantization), but is very slow.

Let us consider a toy problem where a plane is intersecting a voxel grid of size $a \times a \times a = a^3$ cubes. If the plane is axis aligned, it intersects a^2 voxels. A perfect sampling would pick a support point in each intersected voxel, *i.e.*, $|Q| = a^2$ and $a = \sqrt{|Q|}$. Considering that we want $|Q|$ output points, the voxel size v is defined as

$$v = \text{diag} / \sqrt{|Q|} \quad (8)$$

where diag is the diagonal length of the bounding box of the point cloud. This expression is experimentally tested in section 5.2.

5 Experiments

In this section, we evaluate our convolutional layer with respect to the state-of-the-art methods and show that we are competitive with them according to benchmarks for shape classification, part segmentation and semantic segmentation. We also present computation time and memory usage that are in favor of LCP.

Network architectures. In this work, we use a simple yet effective residual network for semantic segmentation. We mimic the architecture of [44], except that ours is designed for k -nn convolution, *i.e.*, we do not need to add phantom points and features to equalize the size of data tensor due to variable number of points in radius search. The network has an encoder-decoder structure. The encoder is composed of an alternation of residual blocks maintaining the resolution and residual blocks with down-sampling. The decoder is a stack of fully-connected and nearest-neighbor upsampling layers. The classification network is the encoder of the previously described network followed by a global average pooling. For large scale semantic segmentation, we use either input modality dropout [44] or dual network fusion [5].

Datasets. We evaluate our convolution on three different tasks: object classification, part segmentation and semantic segmentation.

The classification task is evaluated on ModelNet40 [50]. It contains 12,311 point clouds sampled on CAD models of 40 different categories.

Part segmentation uses Shapenet [52]. It is composed of 16 object category, each category being annotated with 2 to 6 part labels. In our implementation, the network has 50 outputs (one for each part) and loss and scores are computed per object category.

For semantic segmentation, we use two datasets: S3DIS [1], NPM3D [37] and Semantic8 [13]. S3DIS is a subset of the 2D-3D-S Dataset for semantic segmentation of building interiors. The data has been acquired over 6 building floors with an RGBD camera. Points are annotated with 13 labels, *i.e.*, 12 semantic elements (floors, tables, chairs. . .) and a clutter class mostly including office furnitures. The evaluation is done using a 6-fold cross validation. NPM3D is a lidar dataset for large scale outdoor semantic segmentation. Points

were acquired in four cities using a lidar equipped car. 10 urban classes are used for semantic segmentation from impervious surfaces to pools or pedestrians.

Semantic8 dataset is the main dataset of Semantic3D benchmark suite. It contains 30 lidar scenes, 15 for training and 15 for test. Over 4 billion points are labelled with 8 classes such as building, vegetation, and cars, and a challenging class for scanning artifacts. The test set is particularly challenging as it covers a range of diverse scenes: city streets, village or old castles.

Experimental setup. The formalism (and code) allows a variable input size, but in order to use optimization with mini-batches, we train the networks with constant input sizes.

We use 2048 points for classification and part segmentation, and 8192 for semantic segmentation. As the spatial pooling process is stochastic, multiple predictions with the same point cloud might lead to different predictions. We aggregate 16 predictions for each point cloud and select the most predicted shape.

For semantic segmentation, using the whole scene subsampled to 8192 points produces a big loss of information. Instead, we select the points in vertical pillars with a square footprint of 2 m for S3DIS, and 8 m for NPM3D. The center point of the pillar is selected randomly at training time and using a sliding window at test time. If a point is seen several times, the prediction scores are summed and the most probable class is selected afterward.

5.1 Benchmark results

The results are presented in table 1.

On the classification task (table 1(a)) and part segmentation task (table 1(b)), we rank among the best methods: top-3 for classification (only 0.6 point behind the best method); top-2 or top-5 for part segmentation depending on the metric used – mean class intersection over union (mIoU) or instance average intersection over union (mIoU), only 0.3 point mIoU and 0.7 point mIoU behind the best method. It is interesting to notice that we are as good as or better than several methods for which the convolution falls into our formalism, such as ConvPoint [5] or SPLATNet [40].

The semantic segmentation results are presented in table 1(c) for S3DIS, table 1(d) for NPM3D, table 1(e) for Semantic8. We use S3DIS to study the impact of the training strategy. As underlined in [5, 44], direct learning with the colors yields a model relying too much on the color information, at the expense of geometric information. We train three models. The first is the baseline model trained with color information, the second uses color dropout (as in [44]), and the third is a dual model with fusion module [5]. We observe that the third approach gives the best results. In practice, the model trained with modality dropout tends to select one of the two modalities, either color or geometry, depending on what modality gives the best results. On the contrary, the fusion technique uses two networks each trained with a different modality, resulting in a lot larger network, but ensuring that the information of both modalities is taken into account.

Our network with LCP convolutions is second on S3DIS, first on NPM3D and third on Semantic8. On S3DIS, it is the best approach for 3 out of 13 categories and it performs well on the remaining ones. We are only surpassed by KPConv which is radius-search based. On NPM3D, we reach an average intersection over union (av. IoU) of 82.7, 0.7 point before the previously best method. On Semantic8, we place third according to average IoU, and first on overall accuracy among the published and arxiv methods. We obtain the best scores in 3 out of 8 categories (the top-3 for 6 categories out of 8). More interestingly, we exceed the scores of ConvPoint [5] on 5 categories. The only downside is the very low score on the category of artefacts. One possible explanation could be that the architecture used in this paper (the residual network) is not suitable to learn a reject class (the artefact class is mainly all the points that do not belong to the 7 other class, i.e.,

pedestrians but also scanning outliers). It is future work to train the ConvPoint network with our convolution layer to support this hypothesis.

Table 1: Classification and semantic segmentation benchmarks.

(b) ShapeNet

(a) ModelNet40

Methods	OA	AA
<i>Mesh or voxels</i>		
Subvolume [31]	89.2	-
MVCNN [41]	90.1	-
<i>Points</i>		
DGCNN [49]	92.2	90.2
PointNet [30]	89.2	86.2
PointNet++ [32]	90.7	-
PointCNN [22]	92.2	88.1
ConvPoint [5]	92.5	89.6
KPConv [44]	92.9	-
LCP (Ours)	92.3	89.7

Method	mcIoU	mIoU
PointNet++ [32]	81.9	85.1
SubSparseCN [11]	83.3	86.0
SPLATNet [40]	83.7	85.4
SpiderCNN [51]	81.7	85.3
SO-Net [21]	81.0	84.9
PCNN [2]	81.8	85.1
KCNet [39]	82.2	83.7
SpecGCN [46]	-	85.4
RSNet [16]	81.4	84.9
DGCNN [49]	82.3	85.1
SGPN [48]	82.8	85.8
PointCNN [22]	84.6	86.1
ConvPoint [5]	83.4	85.8
KPConv [44]	85.1	86.4
LCP (Ours)	84.8	85.7

(c) S3DIS

Method	Search	IoU	ceiling	floor	wall	beam	col.	wind.	door	chair	table	book.	sofa	board	clut.
Pointnet [30]	Knn	47.6	88.0	88.7	69.3	42.4	23.1	47.5	51.6	42.0	54.1	38.2	9.6	29.4	35.2
RSNet [16]	-	56.5	92.5	92.8	78.6	32.8	34.4	51.6	68.1	60.1	59.7	50.2	16.4	44.9	52.0
PCCN [47]	-	58.3	92.3	96.2	75.9	0.27	6.0	69.5	63.5	65.6	66.9	68.9	47.3	59.1	46.2
SPGraph [19]	Super pt.	62.1	89.9	95.1	76.4	62.8	47.1	55.3	68.4	73.5	69.2	63.2	45.9	8.7	52.9
PointCNN [22]	Knn	65.4	94.8	97.3	75.8	63.3	51.7	58.4	57.2	71.6	69.1	39.1	61.2	52.2	58.6
PointWeb [55]	Knn	66.7	93.5	94.2	80.8	52.4	41.3	64.9	68.1	71.4	67.1	50.3	62.7	62.2	58.5
ShellNet [54]	Knn	66.8	90.2	93.6	79.9	60.4	44.1	64.9	52.9	71.6	84.7	53.8	64.6	48.6	59.4
ConvPoint [5]	Knn	68.2	95.0	97.3	81.7	47.1	34.6	63.2	73.2	75.3	71.8	64.9	59.2	57.6	65.0
KPConv [44]	Radius	70.6	93.6	92.4	83.1	63.9	54.3	66.1	76.6	57.8	64.0	69.3	74.9	61.3	60.3
LCP (Ours <i>RGB only</i>)	Knn	64.9	94.0	97.8	80.5	38.5	48.5	49.8	68.0	79.4	70.7	48.4	43.7	62.9	61.4
LCP (Ours <i>RGB drop.</i>)	Knn	66.6	94.4	97.8	81.5	38.7	43.3	56.4	71.6	80.2	71.8	63.5	54.1	50.6	62.5
LCP (Ours <i>fusion</i>)	Knn	68.4	94.5	98.0	82.9	41.0	46.0	57.8	74.1	77.7	71.7	65.0	60.3	55.0	65.5
Rank		2	3	1	2	7	4	6	2	1	2	3	4	5	1

(d) NPM3D

Method	Av.IoU	Ground	Building	Pole	Bollard	Trash can	Barrier	Pedestrian	Car	Natural
RF MSSF [43]	56.3	99.3	88.6	47.8	67.3	2.3	27.1	20.6	74.8	78.8
MS3 DVS [36]	66.9	99.0	94.8	52.4	38.1	36.0	49.3	52.6	91.3	88.6
HDGCN [24]	68.3	99.4	93.0	67.7	75.7	25.7	44.7	37.1	81.9	89.6
ConvPoint [5]	75.9	99.5	95.1	71.6	88.7	46.7	52.9	53.5	89.4	85.4
KPConv [44]	82.0	99.5	94.0	71.3	83.1	78.7	47.7	78.2	94.4	91.4
LCP (ours <i>fusion</i>)	82.7	99.6	98.1	77.2	91.1	64.7	66.5	58.1	95.6	93.9
Rank	1	1	1	1	1	2	1	2	1	1

Note: We report here only the published methods at the time of writing.

(e) Semantic3D

Method	Av. IoU	OA	Man made	Nat. veg.	High veg.	Low veg.	Build.	Hard scape	Art.	Cars
TML-PC [29]	39.1	74.5	80.4	66.1	42.3	41.2	64.7	12.4	0.	5.8
TMLC-MS [14]	49.4	85.0	91.1	69.5	32.8	21.6	87.6	25.9	11.3	55.3
PointNet++ [32]	63.1	85.7	81.9	78.1	64.3	51.7	75.9	36.4	43.7	72.6
EdgeConv [8]	64.4	89.6	91.1	69.5	65.0	56.0	89.7	30.0	43.8	69.7
SnapNet [4]	67.4	91.0	89.6	79.5	74.8	56.1	90.9	36.5	34.3	77.2
PointGCR [26]	69.5	92.1	93.8	80.0	64.4	66.4	93.2	39.2	34.3	85.3
FPCR [45]	72.0	90.6	86.4	70.3	69.5	68.0	96.9	43.4	52.3	89.5
SPGraph [19]	76.2	92.9	91.5	75.6	78.3	71.7	94.4	56.8	52.9	88.4
ConvPoint [5]	76.5	93.4	92.1	80.6	76.0	71.9	95.6	47.3	61.1	87.7
LCP (ours fusion)	74.6	94.1	94.7	85.2	77.4	70.4	94.0	52.9	29.4	92.6
Rank	3	1	1	1	2	3	5	2	9	1

Note: We report here only the published methods at the time of writing.

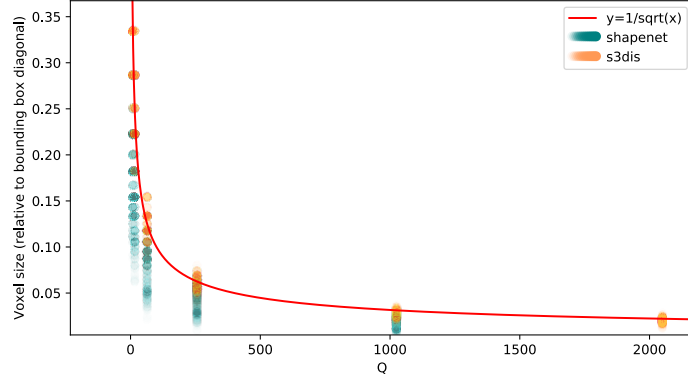


Figure 6: Empirical validation of the voxel size estimation on ShapeNet (blue) and S3DIS (orange). Each dot is the empirical optimal voxel size obtained by dichotomic search. The red line is the voxel size define as the inverse square root of the number of support points.

5.2 Support point sampling: discretization parameter.

Expression (8) has been derived in a very simple case: a point cloud sampled from an axis aligned plane crossing the voxel grid. In practice, planar surfaces are very common, particularly in semantic segmentation (walls, floors, . . .), but are not a good model for most of the object of the scenes (chairs, cars, vegetation, . . .). To validate (8), we compute the optimal quantization parameter (i.e., the parameter with the largest value leading to the desired support point number in a single quantization) computed using a dichotomic search on the parameter space and compare it to the derived expression. Fig. 6 presents the results of the experiment. For each point cloud, the optimal voxel size is represented by a semi-transparent disk (blue for ShapeNet, orange for S3DIS) and can be compared to the derived expression (red curve). In our setting, a curve under the colored disks is not desired (it is an over quantization). We prefer a curve above these disks, i.e., possibly two iterations of the support point selection procedure. We observe that (8) provides a good estimate of the voxel size, especially for S3DIS which is a dataset containing a lot of planes. For ShapeNet, we observe a higher variance, due to the great variability of shapes. We slightly overestimate the voxel size because of numerous objects which cannot be modelled with a plane.

5.3 Support point sampling: computation times.

In order to evaluate the relevance of the proposed sampling approach, we run two experiments. First, in table 2(a), we compare the sampling time as a function of the size of the input point cloud. The number of support points is half the input point cloud size, and the number of neighbors is 16, the scores are averaged over 5000 random points clouds sampled in a cube. We also report the ShapeNet scores to put into perspective the performance and the computation times. We compare our sampling strategy with farthest point sampling [32], the iterative neighborhood rejection [5] and the random baseline. As farthest point sampling [32] is the reference of several state-of-the-art methods, we give the gain relative to this method in percentage.

All timings are given in table 2. Our quantized sampling is almost as fast as random sampling and much more efficient than farthest point sampling. We observe our sampling has almost a linear complexity, compared to farthest point sampling which has a $O(n^2)$ complexity.

Table 2: Timings and memory consumptions.

(a) Computation time of different sampling strategy.

Method	1000 points		Sampling time		10000 points		Shapenet (mIoU)
			5000 points				
Random (baseline)	1.66ms	(-60%)	8.6ms	(-89%)	18.6ms	(-94%)	84.4
ConvPoint [5]	2.60ms	(-37%)	25.4ms	(-68%)	88.2ms	(-71%)	84.6
Farthest [32]	4.12ms	(-)	79.8ms	(-)	310.2ms	(-)	84.7
LCP sampling	1.93ms	(-53%)	10.3ms	(-87%)	20.4ms	(-93%)	84.6

(for n inputs points, $n/2$ support points, 16 neighbors, measured averaged over 5000 iterations.

(b) Timings and memory consumption.

Convolution Layer	Training		Testing		Param. (10^6)
	Time (ms)	Memory (MB)	Time (ms)	Memory (MB)	
ConvPoint	12.2	4283	4.29	1615	10.7
PointCNN* [22]	33.6	3477	6.23	1676	4.5
PCCN* [47]	31.1	4903	10.2	2323	4.2
PCCN** (bs4)	64.2	6379	19.7	2604	18.1
Ours	19.1	5625	4.89	1404	10.7

*: reimplemented in our framework.

**: original formulation with separation trick, differs from the one used for experiments in [47].

5.4 Inference timings and memory consumption

We present in table 2(b) the performance of our convolution layer and compare it to other convolutional layers. All computation times and memory usage are given for the segmentation network architecture and for one point cloud. The measures were done with 8192 points in each point cloud and batch size of 16 (except for PCCN** for which the batch size is reduce to 4 to fit in the GPU memory). Computational times are given per point cloud in milliseconds, and memory usage is reported in mega bytes.

First, we observe at test time that our computation times are very similar to ConvPoint, which is expected as it falls in our formalism. The same would probably be observed for a k -nn version of the KPConv [44].

Then, we can see that PointCNN [22] and PCCN [47] are up to twice slower for inference, even though they have less trainable parameters. PCCN uses separable kernel trick to improve memory performance. In this form, it is similar to N_{out} (N_{out} being the number of filter of the layer) parallel instances of our layer with one kernel element, i.e., it is equivalent to estimate a different \mathbf{A} for each $f \in \{1, \dots, F\}$.

We also report in table 2(b) the performance for PCCN**, the convolution of [47] without the separable kernel which corresponds to a purely continuous convolution described in the paper.

5.5 Filter visualization

The LCP formulation has been designed based on the discrete convolution. 3D filter behavior should be somehow comparable to their 2D counterparts in image processing. In Fig. 7, we represent the outputs of early and late filters for the classification network on ModelNet40. For easy visualization, the results of low level features have been projected on the full resolution point cloud. As expected, early layers produce surface orientation based features: the receptive field at this stage is small. On the contrary, deep layers produces shape-related features corresponding to part recognition, e.g., people head or plane body.

6 Conclusion

We presented a formalism for convolution on point clouds that unifies a good number of proposed convolutional layers. The core of the method is the estimation of a change of space matrix from input points to the kernel space. As opposed to previous methods that use kernel location in space, we simply estimate the

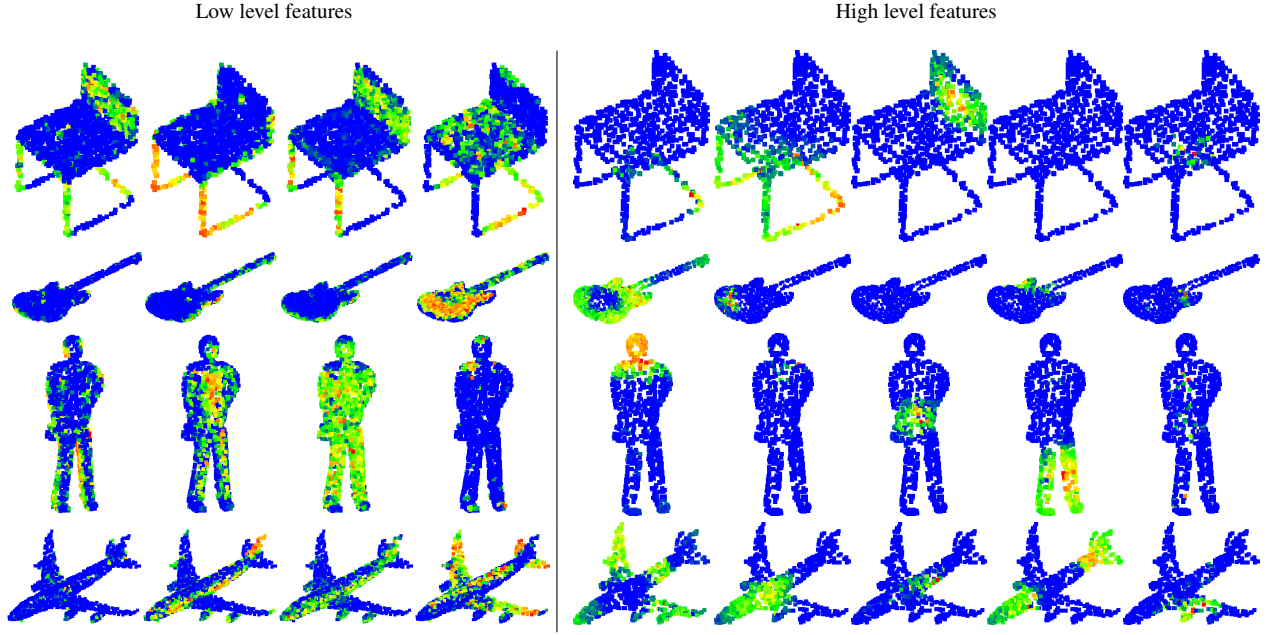


Figure 7: Convolution filter response for different input shape on ModelNet40. Low level features are extracted from the first convolutional layer (four filters), high level ones from the fourth (5 filters). Color map, from blue to red, express the output value of the filter for the corresponding shape.

change of space matrix using an MLP with context aggregation. We also introduce an alternative sampling to the farthest point sampling using a quantization of the local neighborhood. While being almost as efficient, it is almost as fast as random sampling. With these conceptually simple and easy to implement ideas, we obtained the state-of-the-art results among methods based on k -nn search on several benchmarks.

In the course of our experiments, we have also observed that, when RGB information exists, the network tends to focus on this information rather than geometric information. On the contrary, when color is not an input, the geometry is very well exploited (see filter outputs in Fig. 7). To circumvent this problem, we have compared RGB-dropout [44] at training time and two-network fusion [5]. In the first case, the network seems to chose one modality (color or geometry) and not exploit the complementary information. In the second case, the fusion module extracts the best of both modalities but results in a very heavy network. It is a future work to investigate this aspect, for a better extraction of geometric information in conjunction with the other input modality and without using auxiliary networks.

References

- [1] I. Armeni, O. Sener, A. R. Zamir, H. Jiang, I. Brilakis, M. Fischer, and S. Savarese. 3d semantic parsing of large-scale indoor spaces. In *Proceedings of the IEEE Conference on Computer Vision and Pattern Recognition*, pages 1534–1543, 2016.
- [2] M. Atzmon, H. Maron, and Y. Lipman. Point Convolutional Neural Networks by Extension Operators. *arXiv preprint arXiv:1803.10091*, 2018.
- [3] D. Boscaini, J. Masci, E. Rodolà, and M. Bronstein. Learning shape correspondence with anisotropic convolutional neural networks. In *Advances in Neural Information Processing Systems*, pages 3189–3197, 2016.

- [4] A. Boulch, J. Guerry, B. Le Saux, and N. Audebert. SnapNet: 3D point cloud semantic labeling with 2D deep segmentation networks. *Computers & Graphics*, 2017.
- [5] A. Boulch, B. Le Saux, and N. Audebert. Unstructured point cloud semantic labeling using deep segmentation networks. *3DOR*, 2:7, 2017.
- [6] M. M. Bronstein, J. Bruna, Y. LeCun, A. Szlam, and P. Vandergheynst. Geometric deep learning: going beyond euclidean data. *IEEE Signal Processing Magazine*, 34(4):18–42, 2017.
- [7] D. C. Cireřan, U. Meier, J. Masci, L. M. Gambardella, and J. Schmidhuber. Flexible, high performance convolutional neural networks for image classification. In *22nd International Joint Conference on Artificial Intelligence (IJCAI)*, pages 1237–1242. AAAI Press, 2011.
- [8] J. Contreras and J. Denzler. Edge-convolution point net for semantic segmentation of large-scale point clouds. In *IGARSS 2019-2019 IEEE International Geoscience and Remote Sensing Symposium*, pages 5236–5239. IEEE, 2019.
- [9] M. Defferrard, X. Bresson, and P. Vandergheynst. Convolutional neural networks on graphs with fast localized spectral filtering. In *Advances in neural information processing systems*, pages 3844–3852, 2016.
- [10] B. Graham. Spatially-sparse convolutional neural networks. *arXiv preprint arXiv:1409.6070*, 2014.
- [11] B. Graham, M. Engelcke, and L. van der Maaten. 3d semantic segmentation with submanifold sparse convolutional networks. In *Proceedings of the IEEE Conference on Computer Vision and Pattern Recognition*, pages 9224–9232, 2018.
- [12] S. Gupta, R. Girshick, P. Arbeláez, and J. Malik. Learning rich features from rgb-d images for object detection and segmentation. In *European conference on computer vision*, pages 345–360. Springer, 2014.
- [13] T. Hackel, N. Savinov, L. Ladicky, J. D. Wegner, K. Schindler, and M. Pollefeys. SEMANTIC3D.NET: A new large-scale point cloud classification benchmark. In *ISPRS Annals of the Photogrammetry, Remote Sensing and Spatial Information Sciences*, volume IV-1-W1, pages 91–98, 2017.
- [14] T. Hackel, J. D. Wegner, and K. Schindler. Fast semantic segmentation of 3D point clouds with strongly varying density. *ISPRS Annals of Photogrammetry, Remote Sensing & Spatial Information Sciences*, 3(3), 2016.
- [15] B.-S. Hua, M.-K. Tran, and S.-K. Yeung. Pointwise convolutional neural networks. In *Proceedings of the IEEE Conference on Computer Vision and Pattern Recognition*, pages 984–993, 2018.
- [16] Q. Huang, W. Wang, and U. Neumann. Recurrent Slice Networks for 3D Segmentation of Point Clouds. In *Proceedings of the IEEE Conference on Computer Vision and Pattern Recognition*, pages 2626–2635, 2018.
- [17] A. S. J. Bruna, W. Zaremba and Y. LeCun. Spectral networks and locally connected networks on graphs. 2014.
- [18] A. Krizhevsky, I. Sutskever, and G. E. Hinton. Imagenet classification with deep convolutional neural networks. In *25th International Conference on Neural Information Processing Systems (NIPS)*, pages 1097–1105. Curran Associates Inc., 2012.

- [19] L. Landrieu and M. Simonovsky. Large-scale point cloud semantic segmentation with superpoint graphs. In *Proceedings of the IEEE Conference on Computer Vision and Pattern Recognition*, pages 4558–4567, 2018.
- [20] F. J. Lawin, M. Danelljan, P. Tosteberg, G. Bhat, F. S. Khan, and M. Felsberg. Deep projective 3d semantic segmentation. In *International Conference on Computer Analysis of Images and Patterns*, pages 95–107. Springer, 2017.
- [21] J. Li, B. M. Chen, and G. Hee Lee. So-net: Self-organizing network for point cloud analysis. In *Proceedings of the IEEE conference on computer vision and pattern recognition*, pages 9397–9406, 2018.
- [22] Y. Li, R. Bu, M. Sun, W. Wu, X. Di, and B. Chen. Pointcnn: Convolution on x-transformed points. In *Advances in Neural Information Processing Systems*, pages 820–830, 2018.
- [23] Y. Li, D. Tarlow, M. Brockschmidt, and R. Zemel. Gated graph sequence neural networks. *arXiv preprint arXiv:1511.05493*, 2015.
- [24] Z. Liang, M. Yang, L. Deng, C. Wang, and B. Wang. Hierarchical depthwise graph convolutional neural network for 3d semantic segmentation of point clouds. In *2019 International Conference on Robotics and Automation (ICRA)*, pages 8152–8158. IEEE, 2019.
- [25] J. Long, E. Shelhamer, and T. Darrell. Fully convolutional networks for semantic segmentation. In *Proceedings of the IEEE conference on computer vision and pattern recognition*, pages 3431–3440, 2015.
- [26] Y. Ma, Y. Guo, H. Liu, Y. Lei, and G. Wen. Global context reasoning for semantic segmentation of 3d point clouds. In *The IEEE Winter Conference on Applications of Computer Vision*, pages 2931–2940, 2020.
- [27] D. Maturana and S. Scherer. Voxnet: A 3d convolutional neural network for real-time object recognition. In *2015 IEEE/RSJ International Conference on Intelligent Robots and Systems (IROS)*, pages 922–928. IEEE, 2015.
- [28] F. Monti, D. Boscaini, J. Masci, E. Rodola, J. Svoboda, and M. M. Bronstein. Geometric deep learning on graphs and manifolds using mixture model cnns. In *Proceedings of the IEEE Conference on Computer Vision and Pattern Recognition*, pages 5115–5124, 2017.
- [29] J. A. Montoya-Zegarra, J. D. Wegner, L. Ladický, and K. Schindler. Mind the gap: modeling local and global context in (road) networks. In *German Conference on Pattern Recognition*, pages 212–223. Springer, 2014.
- [30] C. R. Qi, H. Su, K. Mo, and L. J. Guibas. PointNet: Deep learning on point sets for 3D classification and segmentation. *Proc. Computer Vision and Pattern Recognition (CVPR), IEEE*, 1(2):4, 2017.
- [31] C. R. Qi, H. Su, M. Nießner, A. Dai, M. Yan, and L. J. Guibas. Volumetric and multi-view cnns for object classification on 3d data. In *Proceedings of the IEEE conference on computer vision and pattern recognition*, pages 5648–5656, 2016.
- [32] C. R. Qi, L. Yi, H. Su, and L. J. Guibas. Pointnet++: Deep hierarchical feature learning on point sets in a metric space. In *Advances in Neural Information Processing Systems*, pages 5105–5114, 2017.

- [33] X. Qi, R. Liao, J. Jia, S. Fidler, and R. Urtasun. 3d graph neural networks for rgb-d semantic segmentation. In *Proceedings of the IEEE International Conference on Computer Vision*, pages 5199–5208, 2017.
- [34] G. Riegler, A. Osman Ulusoy, and A. Geiger. Octnet: Learning deep 3d representations at high resolutions. In *Proceedings of the IEEE Conference on Computer Vision and Pattern Recognition*, pages 3577–3586, 2017.
- [35] O. Ronneberger, P. Fischer, and T. Brox. U-net: Convolutional networks for biomedical image segmentation. In *International Conference on Medical image computing and computer-assisted intervention*, pages 234–241. Springer, 2015.
- [36] X. Roynard, J.-E. Deschaud, and F. Goulette. Classification of point cloud scenes with multiscale voxel deep network. *arXiv preprint arXiv:1804.03583*, 2018.
- [37] X. Roynard, J.-E. Deschaud, and F. Goulette. Paris-lille-3d: A large and high-quality ground-truth urban point cloud dataset for automatic segmentation and classification. *The International Journal of Robotics Research*, 37(6):545–557, 2018.
- [38] F. Scarselli, M. Gori, A. C. Tsoi, M. Hagenbuchner, and G. Monfardini. The graph neural network model. *IEEE Transactions on Neural Networks*, 20(1):61–80, 2008.
- [39] Y. Shen, C. Feng, Y. Yang, and D. Tian. Mining point cloud local structures by kernel correlation and graph pooling. In *Proceedings of the IEEE Conference on Computer Vision and Pattern Recognition*, volume 4, 2018.
- [40] H. Su, V. Jampani, D. Sun, S. Maji, E. Kalogerakis, M.-H. Yang, and J. Kautz. Splatnet: Sparse lattice networks for point cloud processing. In *Proceedings of the IEEE Conference on Computer Vision and Pattern Recognition*, pages 2530–2539, 2018.
- [41] H. Su, S. Maji, E. Kalogerakis, and E. Learned-Miller. Multi-view convolutional neural networks for 3d shape recognition. In *Proceedings of the IEEE international conference on computer vision*, pages 945–953, 2015.
- [42] M. Tatarchenko, J. Park, V. Koltun, and Q.-Y. Zhou. Tangent convolutions for dense prediction in 3d. In *Proceedings of the IEEE Conference on Computer Vision and Pattern Recognition*, pages 3887–3896, 2018.
- [43] H. Thomas, F. Goulette, J.-E. Deschaud, and B. Marcotegui. Semantic classification of 3d point clouds with multiscale spherical neighborhoods. In *2018 International Conference on 3D Vision (3DV)*, pages 390–398. IEEE, 2018.
- [44] H. Thomas, C. R. Qi, J.-E. Deschaud, B. Marcotegui, F. Goulette, and L. J. Guibas. Kpconv: Flexible and deformable convolution for point clouds. *arXiv preprint arXiv:1904.08889*, 2019.
- [45] G. Truong, S. Z. Gilani, S. M. S. Islam, and D. Suter. Fast point cloud registration using semantic segmentation. In *2019 Digital Image Computing: Techniques and Applications (DICTA)*, pages 1–8. IEEE, 2019.
- [46] C. Wang, B. Samari, and K. Siddiqi. Local Spectral Graph Convolution for Point Set Feature Learning. *arXiv preprint arXiv:1803.05827*, 2018.

- [47] S. Wang, S. Suo, W.-C. Ma, A. Pokrovsky, and R. Urtasun. Deep parametric continuous convolutional neural networks. In *Proceedings of the IEEE Conference on Computer Vision and Pattern Recognition*, pages 2589–2597, 2018.
- [48] W. Wang, R. Yu, Q. Huang, and U. Neumann. SGPN: Similarity group proposal network for 3D point cloud instance segmentation. In *Proceedings of the IEEE Conference on Computer Vision and Pattern Recognition*, pages 2569–2578, 2018.
- [49] Y. Wang, Y. Sun, Z. Liu, S. E. Sarma, M. M. Bronstein, and J. M. Solomon. Dynamic graph CNN for learning on point clouds. *arXiv preprint arXiv:1801.07829*, 2018.
- [50] Z. Wu, S. Song, A. Khosla, F. Yu, L. Zhang, X. Tang, and J. Xiao. 3d shapenets: A deep representation for volumetric shapes. In *Proceedings of the IEEE conference on computer vision and pattern recognition*, pages 1912–1920, 2015.
- [51] Y. Xu, T. Fan, M. Xu, L. Zeng, and Y. Qiao. Spidercnn: Deep learning on point sets with parameterized convolutional filters. In *Proceedings of the European Conference on Computer Vision (ECCV)*, pages 87–102, 2018.
- [52] L. Yi, V. G. Kim, D. Ceylan, I. Shen, M. Yan, H. Su, C. Lu, Q. Huang, A. Sheffer, L. Guibas, et al. A scalable active framework for region annotation in 3D shape collections. *ACM Transactions on Graphics (TOG)*, 35(6):210, 2016.
- [53] L. Yi, H. Su, X. Guo, and L. J. Guibas. Syncspeccnn: Synchronized spectral cnn for 3d shape segmentation. In *Proceedings of the IEEE Conference on Computer Vision and Pattern Recognition*, pages 2282–2290, 2017.
- [54] Z. Zhang, B.-S. Hua, and S.-K. Yeung. Shellnet: Efficient point cloud convolutional neural networks using concentric shells statistics. In *Proceedings of the IEEE International Conference on Computer Vision*, pages 1607–1616, 2019.
- [55] H. Zhao, L. Jiang, C.-W. Fu, and J. Jia. Pointweb: Enhancing local neighborhood features for point cloud processing. In *Proceedings of the IEEE Conference on Computer Vision and Pattern Recognition*, pages 5565–5573, 2019.
- [56] Y. Zhou and O. Tuzel. VoxelNet: End-to-end learning for point cloud based 3D object detection. In *IEEE Conference on Computer Vision and Pattern Recognition (CVPR)*, pages 4490–4499, Salt Lake City, UT, USA, 2018.

Supplementary material

We present complementary information about the LightConvPoint paper. First, in section A, we detail the network architectures used for classification and semantic segmentation. Then, in section B, we discuss the use of a learned normalization of the support point neighborhoods. Finally, in section C, we provide more qualitative results on the semantic segmentation test datasets.

A Network details.

As presented in section 5.1 of the paper, we use the residual architecture inspired from [44], except that we use the LCP convolution and k nn search.

Residual block. The residual block (Fig. 8(a)) is the core element of our network. An LCP layer is placed between two linear layers. The residual connection has one “optional” linear layer and one “optional” max-pooling layer. These “optional” layers are used only if the number of input channels is different from the number of output channels (linear layer) or if the cardinality of the support points is different from the cardinality of the input point clouds (max pooling).

Classification and segmentation network. The two networks are presented in Fig. 8(b). They share the same encoder structure, i.e., an LCP layer and 9 residual blocks with progressive reduction of the point cloud size.

The classification network has an extra point-wise fully connected (or unary convolutional) layer to fit the number of desired classes. The final prediction is done by averaging the scores of the 8 remaining points after encoding.

The segmentation network has an encoder-decoder structure. The decoder is a stack of 5 unary layers with nearest-neighbor up-sampling in-between. We use skip connections from the encoder to the decoder: the target points for up-sampling are the points at the corresponding scale in the encoder, we also concatenate features from the encoder and the decoder at each scale.

Fusion network. The fusion network (Fig. 8(c)) is the network from the official repository of ConvPoint [5]. It is composed of 3 layers: 2 convolution and one unary layer. The features from the penultimate layer of both segmentation networks are concatenated and given to the fusion module. Its predictions, along with the predictions of the two segmentation networks, are finally concatenated in a last fully-connected layer.

Parameters of the convolution. In order to keep the setup simple, we use the same parameters for all the LCP convolution layers. The neighborhood size of the support points is fixed to 16 and we also use 16 kernel elements. (Note that both in the formalism and in the code, these two parameters can have different values). In the encoder, each residual block with stride reduces the number of support points. The number of points is reduced from $|P|$ to 512, then 128, then 32 and finally 8.

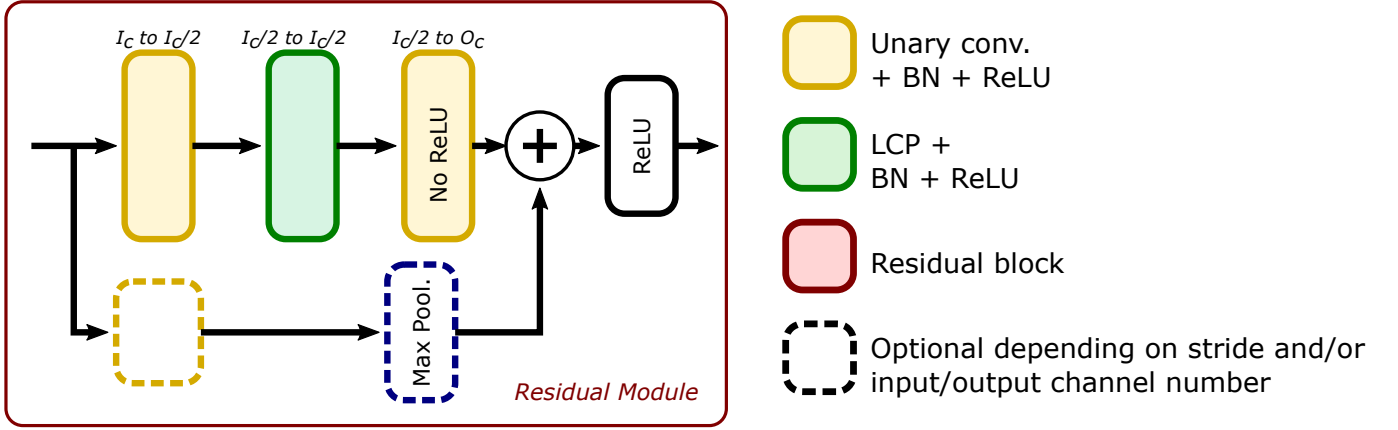
B K -nearest-neighbor search with learned relaxed neighborhood normalization

In the paper, we describe the neighborhood normalization with an estimated average neighborhood size:

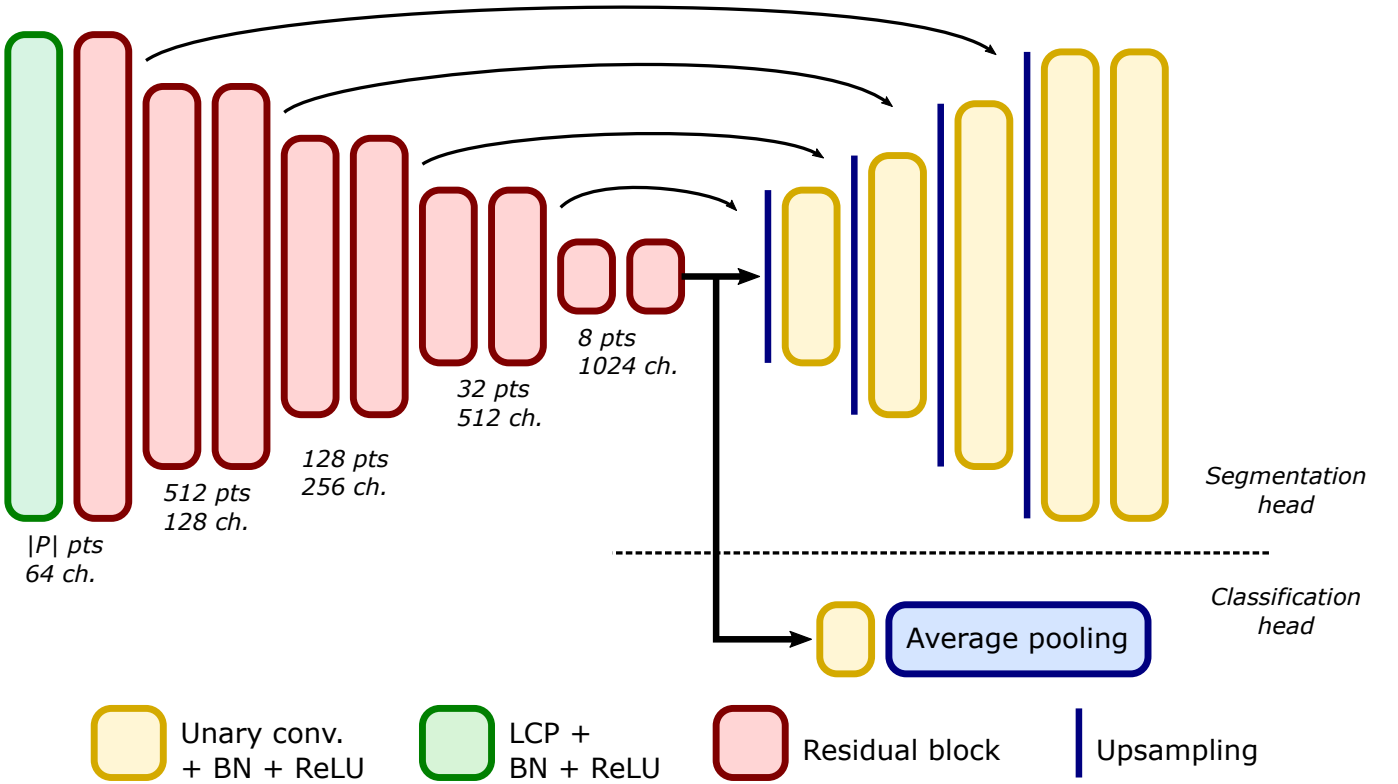
$$r_t = \hat{r} * m + r_{t-1} * (1 - m) \quad (9)$$

and a learned weighting function for the points with respect to the relative distance x to the support point:

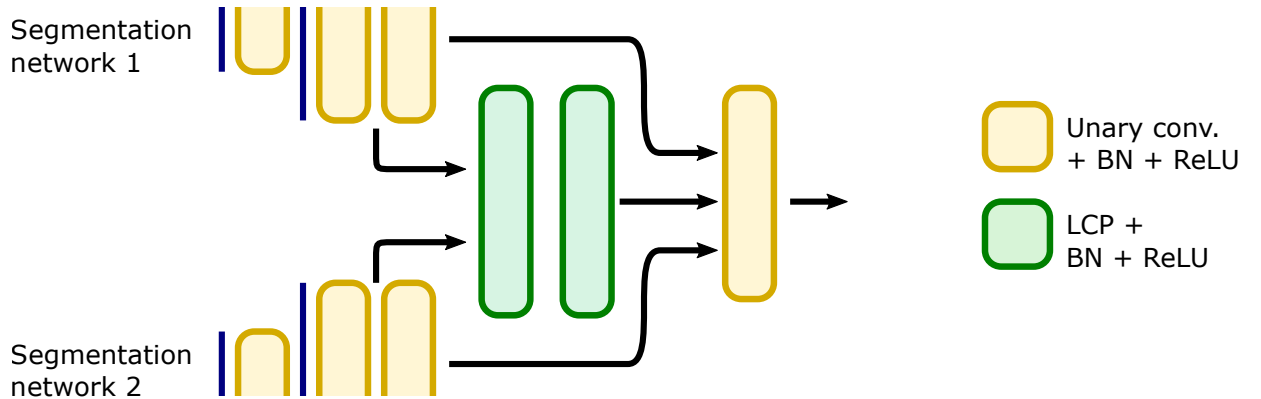
$$w(x) = \sigma(\beta - \alpha x) \quad (10)$$



(a) Residual block.



(b) Classification and segmentation networks.



(c) Fusion network.

Figure 8: Network architectures used for semantic segmentation and classification.

where w is the weight associated to distance x , $\sigma(\cdot)$ is the sigmoid function, β is the parameter defining the window size and α is the smoothness factor of the window. Both parameters α and β are learned.

In this section, we observe the behavior of this constitutive part of our convolutional layer depending on the dataset and on the layer depth in the network.

Average neighborhood radius at each layer. First, we study the estimated neighborhood size at each level of the encoder. This size is the radius of the sphere encompassing the 16 points of the neighborhood. We plot the evolution of this radius in Fig. 9(a) for different datasets.

As expected, the radius of the neighborhood sphere is directly linked to the input point cloud dimensions in the 3D space, i.e., to the size of the point cloud pillars (vertical infinite cylinders of size 8 meters for Semantic8 and NPM3D, and 2 meters for S3DIS) or the scale of the CAD models of ShapeNet (these models are scaled to fit into the unit sphere).

Weighting function. In Fig. 9(b) and (c), we plot the α and β parameters at each LCP layer of the network. First, we observe that these parameters, that optimized with the network, take different values that are not the initial value before network optimization ($\alpha = 1$ and $\beta = 1$). Second, we can draw the same conclusion as in the previous paragraph: Semantic8 and NPM3D, which share common properties (outdoor, same pillar size, similar scenes (mostly urban)), have similar α and β behaviors, while it differs with the other datasets. Third, we observe the same global behavior: α tends to decrease and β to increase with the layer depth. As a result, the weighting function w becomes wider and flatter in deeper layers, i.e., more permissive.

We illustrate this phenomenon on Figs. 9(d-e), where we represent the weighting function after optimization for the first and the seventh LCP layer of the network (we normalize the curves for comparison purposes). The black curve is the initial w function, before optimization.

At the first layer, only the points very close to the support point have an influence on the matrix \mathbf{A} . To our understanding, in the absence of noise in the data, it relates to the fact that a small neighborhood is sufficient to estimate local geometric features.

On the contrary, in the deeper layer, all the points participate to \mathbf{A} . At this stage, the size of the point cloud is small and each point carries features that are discriminative for the task. The network considers all available information, including points that are faraway from the support points. For example, wing extremities can be faraway from the center of a plane.

Influence on the performances. To provide quantitative figures of the impact of the relaxed neighborhood normalization and weighting, we trained a segmentation network in two configurations: with unit ball normalization and with our normalization (with the corrected version of the network, without the error described in the Erratum section at the beginning of this document). The results, reported in Table 3, show an increase of the mean class intersection over union (mIoU) by 0.2 point and of the instance average intersection over union (mIoU) by 0.1 point. This gain is small but significative for the dataset.

Table 3: Evaluation of the impact of the relaxed neighborhood normalization and weighting on the ShapeNet dataset.

Method	mIoU	mIoU
Baseline (normalization to unit ball)	84.6	85.6
Relaxed normalization and weighting (ours)	84.8	85.7

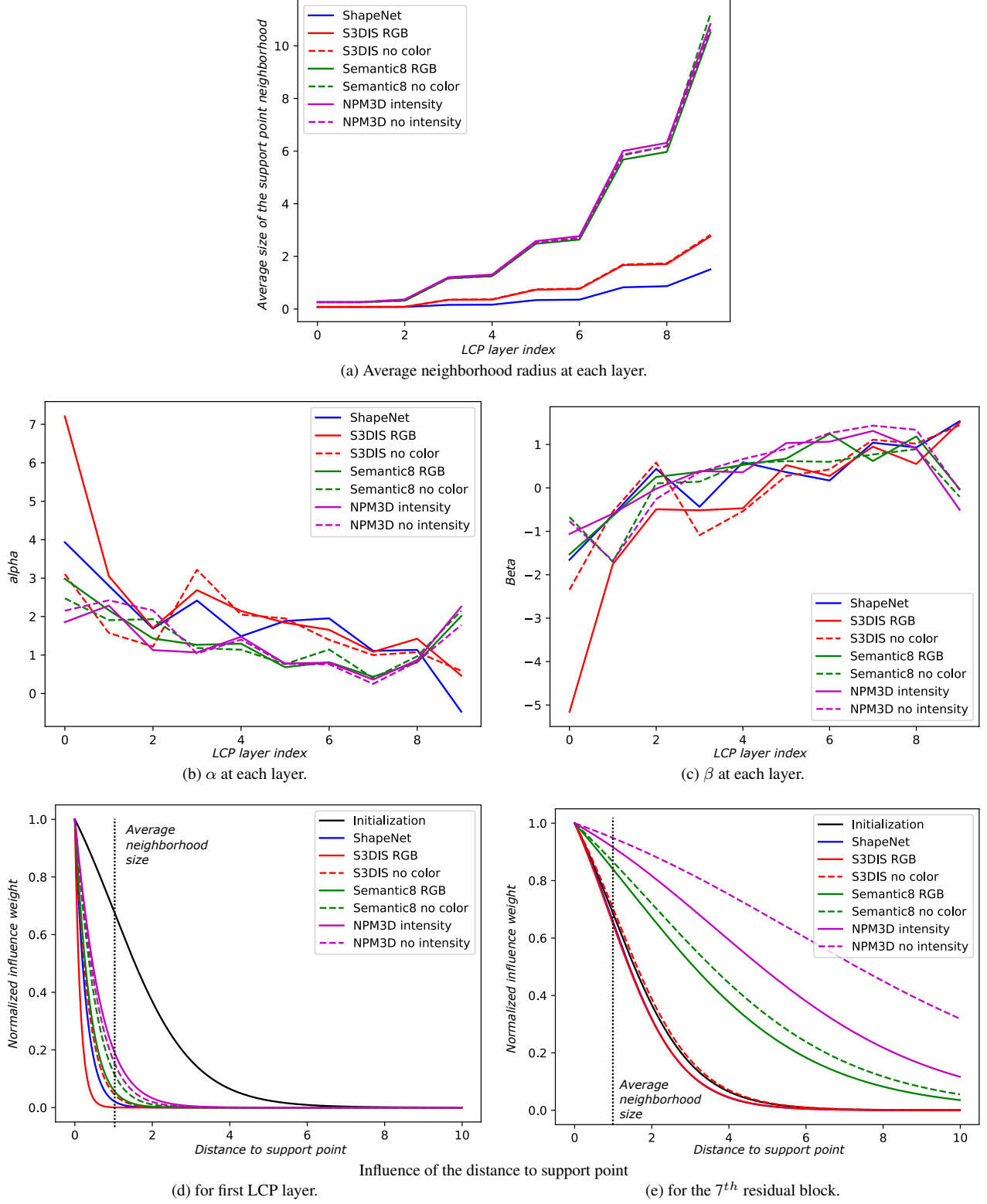


Figure 9: Behavior of the relaxed neighborhood normalization and weighting across the segmentation network for various datasets.

C Qualitative results of segmentation

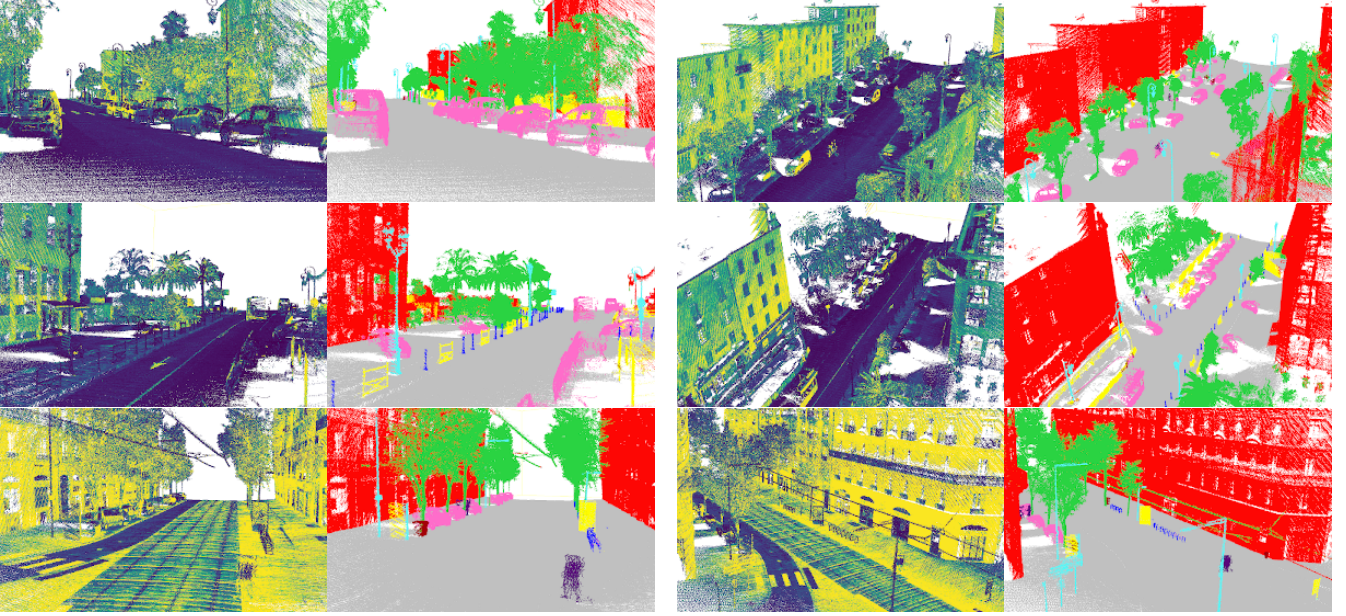


Figure 10: Visual results of our predictions on the test scenes of the NPM3D dataset.

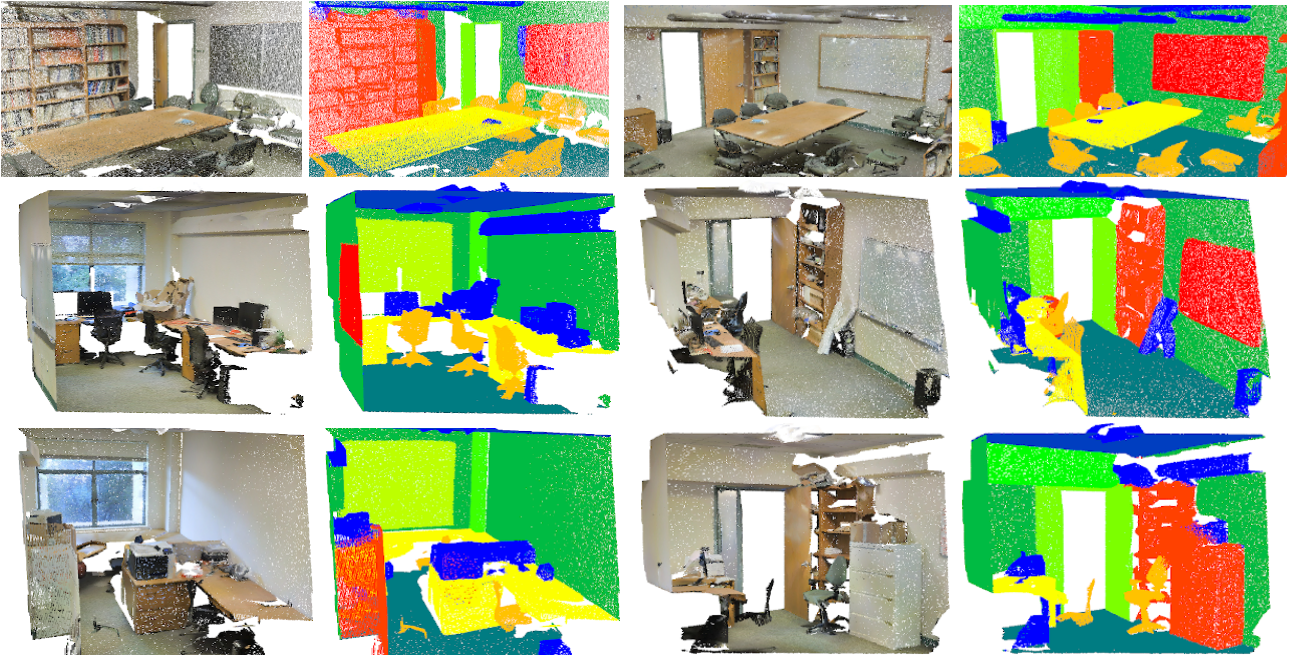


Figure 11: Visual results of our predictions on the S3DIS dataset.

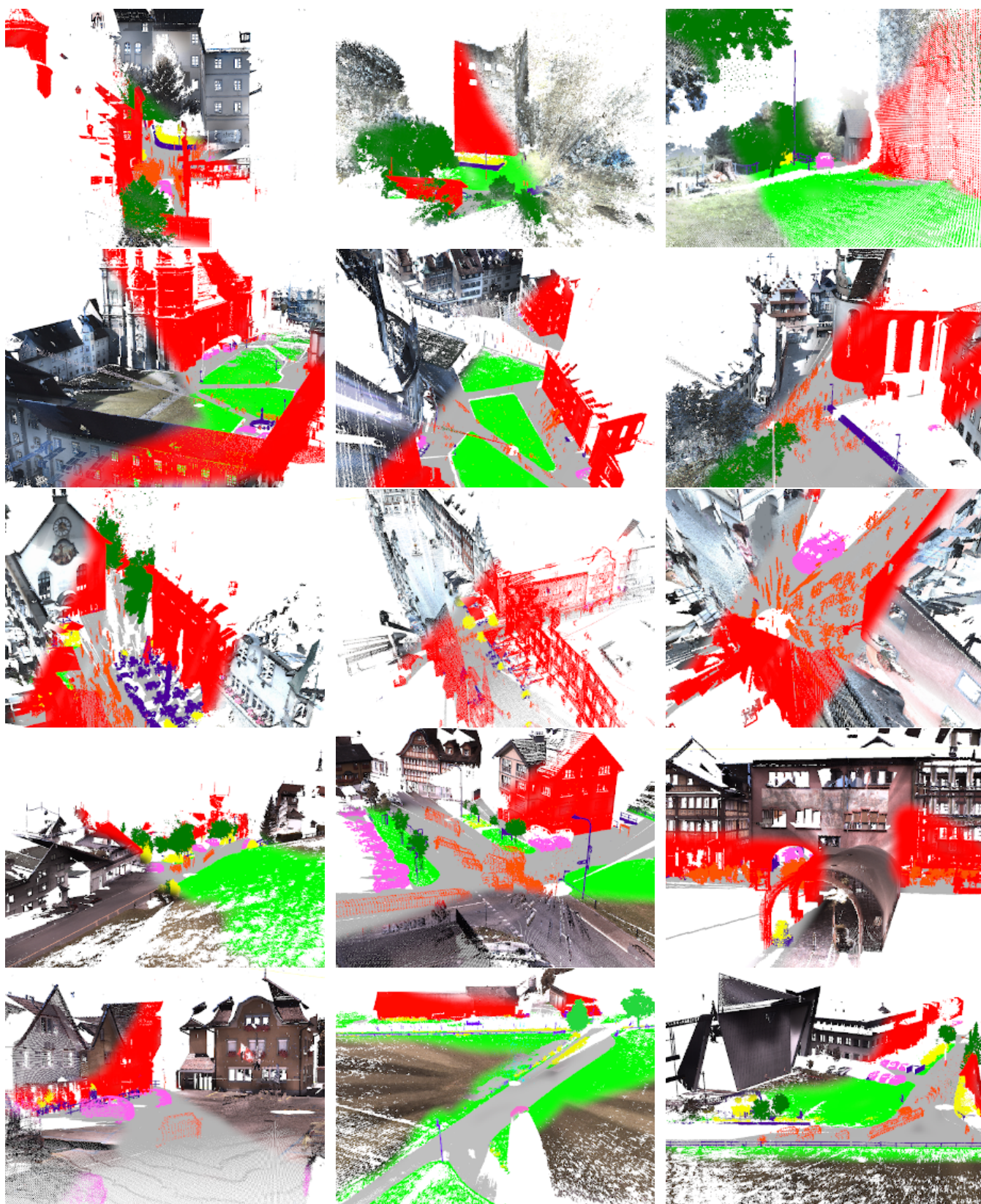


Figure 12: Visual results of our predictions on the 15 test scenes of the Semantic8 dataset.